

# Constraining the Luminosity Function and Delay-Time Distribution of Short Gamma-Ray Bursts for Multimessenger Gravitational-Wave Detection Rate Estimation

Chong-Yu Gao,<sup>1,2</sup> Jun-Jie Wei<sup>1,2\*</sup> and Hou-Dun Zeng<sup>1,3</sup>

<sup>1</sup>*Purple Mountain Observatory, Chinese Academy of Sciences, Nanjing 210023, China*

<sup>2</sup>*School of Astronomy and Space Sciences, University of Science and Technology of China, Hefei 230026, China*

<sup>3</sup>*Key Laboratory of Dark Matter and Space Astronomy Purple Mountain Observatory, Chinese Academy of Sciences Nanjing, 210023, China*

Accepted XXX. Received YYY; in original form ZZZ

## ABSTRACT

In this work, we analyze the most recent short gamma-ray burst (sGRB) sample detected by the *Fermi* satellite to reassess the sGRB luminosity function and formation rate. Using the empirical redshift-luminosity correlation, we first determine the pseudo redshifts of 478 sGRBs. Then, we use the maximum likelihood method to constrain the luminosity function and formation rate of sGRBs under various delay-time distribution models, finding the Gaussian delay model statistically preferred over the power-law and lognormal delay models based on the Deviance Information Criterion. The local formation rate of sGRBs is  $R_{\text{sGRB}}(0) = 1.37^{+0.30}_{-0.27} \text{ Gpc}^{-3} \text{ yr}^{-1}$ , largely independent of the adopted delay-time distribution model. Additionally, we investigate the potential for joint detection of sGRBs and their gravitational wave (GW) counterparts from binary neutron star mergers using both current and future GRB and GW facilities. For sGRB detection, we consider three existing satellites: *Fermi*, the Space-based multi-band astronomical Variable Objects Monitor (*SVOM*), and the Einstein Probe (*EP*). For GW detection, we examine two International GW Networks (IGWN): a four-detector network consisting of LIGO Hanford, Livingston, Virgo, and KAGRA (IGWN4) and an upcoming five-detector network that includes these four detectors plus LIGO India (IGWN5). Incorporating the angular dependence of sGRB jet emission energy, our results show that for different delay-time distribution models, the joint sGRB and GW detection rates for *Fermi*, *SVOM*, and *EP* with IGWN4 (IGWN5) lie within  $0.19\text{--}0.27 \text{ yr}^{-1}$  ( $0.93\text{--}1.35 \text{ yr}^{-1}$ ),  $0.07\text{--}0.10 \text{ yr}^{-1}$  ( $0.51\text{--}0.79 \text{ yr}^{-1}$ ), and  $0.01\text{--}0.03 \text{ yr}^{-1}$  ( $0.15\text{--}0.27 \text{ yr}^{-1}$ ), respectively.

**Key words:** gamma-ray bursts – gravitational waves – neutron star mergers – methods: statistical

## 1 INTRODUCTION

Gamma-ray bursts (GRBs) are the most energetic explosions in the Universe. They are typically divided into two groups based on a critical duration value of  $T_{90} = 2$  seconds (Kouveliotou et al. 1993). Long GRBs are generally believed to originate from the core collapses of massive stars (Woosley 1993), whereas short GRBs (sGRBs) are thought to result from the mergers of two compact objects, such as neutron stars (NSs) or black holes (BHs) (Eichler et al. 1989). The multimessenger observations of the gravitational wave event (GW170817) and its associated sGRB (GRB 170817A) from a binary neutron star (BNS) merger have provided compelling evidence supporting the compact star merger origin of sGRBs (Abbott et al. 2017; Goldstein et al. 2017; Savchenko et al. 2017). Moreover, the abundant multiwavelength follow-up observations of the afterglow of GRB 170817A also spurred extensive research into the jet structure and the radiation processes of sGRBs (Troja et al. 2017; Lyman et al. 2018; Margutti et al. 2018; Mooley et al. 2018a,b; Troja et al. 2018; Ghirlanda et al. 2019; Beniamini et al. 2020a,b; Troja et al. 2020).

The multimessenger joint observations of gravitational waves

(GWs) and sGRBs provide valuable information about the jet launching time and the propagation of the jet through the ejecta. Therefore, these observations are an ideal probe to understand not only the sGRB sources but also the jet dynamics and the emission mechanism (Nakar 2007; Berger 2014; Nakar 2020). However, aside from GW170817/GRB 170817A, no other joint GW and sGRB detections have been identified, which hinders the advancement of our understanding of the sGRB origins and the jet mechanism.

The formation rate of sGRBs is directly related to the expected number of GW events associated with sGRBs for the current and upcoming high-energy GRB and GW facilities. However, the number of sGRBs with redshift measurements is very small, making it difficult to estimate the sGRB formation rate. Due to the small sample size, previous studies estimated the local sGRB formation rate to range from  $0.1 \text{ Gpc}^{-3} \text{ yr}^{-1}$  to  $400 \text{ Gpc}^{-3} \text{ yr}^{-1}$  (Guetta & Piran 2005, 2006; Nakar et al. 2006a; Guetta & Stella 2009; Dietz 2011; Petrillo et al. 2013; Siellez et al. 2014; Sun et al. 2015; Ghirlanda et al. 2016; Liu & Yu 2019; Dainotti et al. 2021; Dimitrova et al. 2023). Using the empirical correlation between the spectral peak energy  $E_p$  and the peak luminosity  $L$  (Yonetoku et al. 2004; Tsutsui et al. 2013), Yonetoku et al. (2014) determined the pseudo redshifts of those sGRBs without a known redshift, thereby enlarging the available sGRB sample. Then they derived the luminosity function (LF) and formation

\* E-mail: jjwei@pmo.ac.cn

rate of sGRBs by using the non-parametric Lynden-Bell  $c^-$  method (see also [Zhang & Wang 2018](#)). Keep in mind that the Lynden-Bell  $c^-$  method necessitates a certain uniformity in data coverage to be applicable ([Lynden-Bell 1971](#)). In reality, however, sGRB data suffer from the truncation of the flux limit of the detector, and the detector's sensitivity is hard to parametrize, making it challenging to construct a uniformly distributed sample of sGRBs. Maximum-likelihood algorithms ([Marshall et al. 1983](#)) are preferable for addressing the sGRB problem because they are less constrained by the conditions of a given sample and offer greater flexibility in modeling systematic uncertainties. In this study, we follow the treatment of [Yonetoku et al. \(2014\)](#) and [Zhang & Wang \(2018\)](#) to first obtain the pseudo redshifts of sGRBs observed by *Fermi* using the  $E_p$ - $L$  correlation. To account for systematics and unknowns in our statistical analysis, we then employ the maximum likelihood method to examine the enlarged sGRB sample, thereby constraining the LF and formation rate of sGRBs.

With the derived LF and formation rate of sGRBs, we can further investigate the joint detection prospects of sGRBs and their GW counterparts using GRB and GW facilities. The success of joint GW and sGRB detections depends on the sensitivities and capabilities of both GW detectors and GRB missions. Currently, the fourth observation (O4) run of the International Gravitational Wave Network-4 (IGWN4), which includes four detectors—Advanced LIGO Livingston and Hanford ([LIGO Scientific Collaboration et al. 2015](#)), Advanced Virgo ([Acerne et al. 2015](#)), and KAGRA at design sensitivity ([Aso et al. 2013](#))—is ongoing. In the future, the LIGO detectors at Livingston and Hanford will be upgraded to A+ sensitivity ([Barsotti et al. 2018](#)), and the planned GW detector LIGO-India ([Iyer et al. 2011; Saleem et al. 2022](#)) will joint the detector network, forming the International Gravitational Wave Network-5 (IGWN5). This IGWN5 network will significantly enhance the GW detection capabilities of its detectors. As the sensitivity and detection horizon of GW detectors continue to improve significantly, the primary limitation for joint detections is likely to soon be the sensitivity of GRB detectors such as *Fermi*. Recently, the Space-based multi-band astronomical Variable Objects Monitor (*SVOM*; [Atteia et al. 2022](#)) and the Einstein Probe (*EP*; [Yuan et al. 2022](#)) have been launched into space. Both satellites share the important scientific objective of detecting the electromagnetic counterparts of GWs. Estimating the expected detection rates of sGRB associated with GWs for these two missions will be crucial for subsequent observational plans and related research.

Several studies have aimed to estimate joint GW-sGRB detection rates. [Howell et al. \(2019\)](#) estimated that Advanced LIGO at design sensitivity could detect up to  $\sim 4 \text{ yr}^{-1}$  joint GW-sGRB events, increasing to  $\sim 10 \text{ yr}^{-1}$  with the A+ upgrade. For the fourth observing run (O4) of the LIGO-Virgo-KAGRA network, [Colombo et al. \(2022\)](#) projected joint detection rates of  $\sim 0.03 \text{ yr}^{-1}$  and  $\sim 0.17 \text{ yr}^{-1}$  using *Swift* and *Fermi*, respectively. Similarly, [Patricelli et al. \(2022\)](#) reported rates up to  $\sim 6 \text{ yr}^{-1}$  with *Fermi* during O4, while [Salafia et al. \(2023\)](#) predicted 0.2–1.3 detectable GW-sGRB events per year for *Fermi*/GBM and the Advanced GW detector network during O4. [Bhattacharjee et al. \(2024\)](#) found that for different jet structure models, joint GW-sGRB detection rates for *Fermi* and *Swift* with IGWN4 (IGWN5) range from  $0.07$ – $0.62 \text{ yr}^{-1}$  ( $0.8$ – $4.0 \text{ yr}^{-1}$ ) and  $0.02$ – $0.14 \text{ yr}^{-1}$  ( $0.15$ – $1.0 \text{ yr}^{-1}$ ), respectively.

In this work, we analyze the most recent sGRB sample detected by *Fermi*'s Gamma-ray Burst Monitor (*Fermi*/GBM) to determine the LF and formation rate of sGRBs through the application of the maximum likelihood method. Then, we explore the potential for joint sGRB and GW detections from BNS mergers using existing and upcoming GRB and GW facilities. For sGRB detection, we consider

three existing satellites: *Fermi*, *SVOM*, and *EP*. For GW detection, we consider two GW detector networks: the current IGWN4 and the upcoming IGWN5. Discussions have been held regarding sGRB-like emissions from NS-BH mergers; however, the theoretical aspects remain unclear, and there is currently no observational confirmation. Therefore, we exclude NS-BH mergers from our analysis.

This paper is organized as follows. In Section 2, we describe the *Fermi*/GBM sample available to us, and obtain the pseudo redshifts of sGRBs. In Section 3, the LF and formation rate of sGRBs are determined through the maximum likelihood method. The synthetic BNS population model, the sGRB detection rates, and the prospects of joint sGRB and GW detections are presented in Section 4. Finally, we provide a brief summary and discussion in Section 5. Throughout this paper, we assume a standard  $\Lambda$ CDM cosmological model and adopt the parameters of  $H_0 = 67.4 \text{ km s}^{-1} \text{ Mpc}^{-1}$ ,  $\Omega_m = 0.315$ , and  $\Omega_\Lambda = 1 - \Omega_m = 0.315$  ([Planck Collaboration et al. 2020](#)).

## 2 FERMI GRB SAMPLE AND REDSHIFT ESTIMATION

### 2.1 Sample selection

Since the launch of the *Fermi* satellite on 2008 June, 3671 GRBs have been detected up to 2023 December 15. We select 553 sGRBs with durations  $T_{90} < 2 \text{ s}$  in the observer frame. For each sGRB, we download the 64 ms peak photon flux  $P$  (in units of photons  $\text{cm}^{-2} \text{ s}^{-1}$ ) in the 10–1000 keV energy band and the spectral parameters (including the low- and high-energy photon indices  $\alpha$  and  $\beta$ , and the observed peak energy  $E_p$ ) from the online *Fermi*/GBM burst catalog ([Gruber et al. 2014; von Kienlin et al. 2014; Narayana Bhat et al. 2016; von Kienlin et al. 2020](#)).<sup>1</sup> Figure 1 shows the peak-flux distribution of all the 553 sGRBs, ranging from  $1.91$  to  $3198.53 \text{ photons cm}^{-2} \text{ s}^{-1}$ .

The *Fermi*/GBM trigger mechanism is complex, and its sensitivity to GRBs is difficult to parametrize precisely. In practice, not all faint GRBs with peak fluxes slightly above the *Fermi*/GBM detection threshold are successfully triggered. As shown in Figure 1, the peak-flux distribution deviates notably from an ideal power law at the lower end due to incomplete sampling of faint bursts. To address this, we fit the peak-flux distribution with a simple power law and find that bursts with peak fluxes greater than  $4.1 \text{ photons cm}^{-2} \text{ s}^{-1}$  are well described by a power-law distribution. To avoid complications arising from a detailed treatment of the *Fermi*/GBM trigger, we focus on a sample of 512 sGRBs with peak fluxes of  $P \geq 4.1 \text{ photons cm}^{-2} \text{ s}^{-1}$ . Indeed, above the flux limit ( $P_{\lim} = 4.1 \text{ photons cm}^{-2} \text{ s}^{-1}$ ), the instrumental selection effects leading to incomplete sampling are negligible (see Figure 1). Thus, we assume that the trigger efficiency for bursts with  $P \geq P_{\lim}$  is 100%.

### 2.2 Redshift estimation for sGRBs

The current number of sGRBs with redshift measurements is very small. In order to study their LF and formation rate, we determine the pseudo redshifts of sGRBs observed by *Fermi*/GBM using the empirical correlation between the observer-frame spectral peak energy ( $E_p$ ) and the source-frame peak bolometric luminosity ( $L$ ) ([Tsutsui et al. 2013; Zhang & Wang 2018](#)). This correlation is given by ([Zhang](#)

<sup>1</sup> <https://heasarc.gsfc.nasa.gov/W3Browse/fermi/fermigbrst.html>

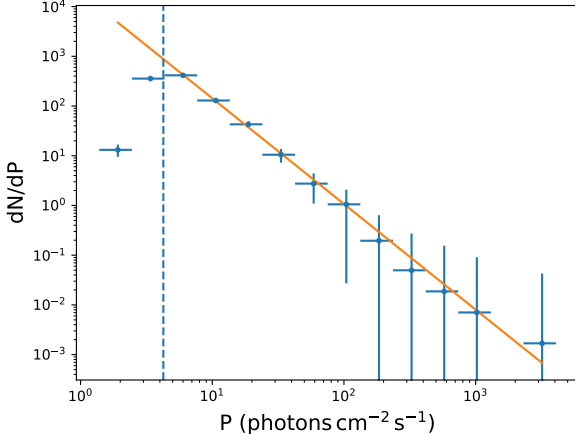


**Figure 1.** The peak-flux distribution of 553 sGRBs detected by *Fermi*/GBM. The vertical dashed line stands for the limiting flux ( $\sim 4.1$  photons  $\text{cm}^{-2} \text{s}^{-1}$ ) above which the instrumental selection effects on incomplete sampling of faint bursts become negligible. The solid line represents the best power-law fit to the peak-flux distribution for  $P \geq 4.1$  photons  $\text{cm}^{-2} \text{s}^{-1}$ .

& Wang 2018)

$$L = (7.15 \pm 0.49) \times 10^{50} \left[ \frac{E_p(1+z)}{100 \text{ keV}} \right]^{1.63 \pm 0.03}, \quad (1)$$

which can be rewritten as

$$\frac{d_l^2(z)}{(1+z)^{1.63}} = \frac{7.15 \times 10^{50}}{4\pi F_p} \left( \frac{E_p}{100 \text{ keV}} \right)^{1.63}, \quad (2)$$

where  $d_l$  is the luminosity distance and  $F_p$  is the source-frame peak bolometric flux at 64 ms time intervals (in units of  $\text{erg cm}^{-2} \text{s}^{-1}$ ). The pseudo redshift of each burst can be estimated using the spectral parameters of the Band function (Band et al. 1993) and the 64 ms peak photon flux  $P$  in the 10–1000 keV observer-frame energy band. With the pseudo redshift, we can further calculate the peak bolometric luminosity  $L$  in the 1–10<sup>5</sup> keV source-frame energy range. In our calculations, we adopt the spectral parameters from the *Fermi*/GBM burst catalog. Our sample contains 181 sGRBs without spectral parameter measurements. For these events, we set  $\alpha = -1$  and  $\beta = -2.25$  (Preece et al. 2000; Kaneko et al. 2006), while  $E_p$  is randomly drawn from the observed distribution of *Fermi* sGRBs with spectral measurements. Paul (2018a) demonstrated that this method statistically reproduces the pseudo redshifts of long GRBs with known redshifts. This approach is justified because *Fermi*/GBM, as a wide-band detector, samples the  $E_p$  space with minimal energy-dependent selection bias. Furthermore, Paul (2018b) applied this method to estimate the pseudo redshifts of sGRBs. The pseudo redshift–luminosity distribution of 512 sGRBs is shown in Figure 2. Since the maximum redshift observed for sGRBs is 2.609, we exclude those bursts with pseudo-redshifts  $z > 3$ . Hereafter, we use 478 sGRBs with  $P \geq 4.1$  photons  $\text{cm}^{-2} \text{s}^{-1}$  and  $z \leq 3$  for further analysis.

Among our final sample of 478 sGRBs, 18 bursts have spectroscopically confirmed redshifts. In Table 1, we list the measured redshifts and pseudo-redshift estimates for these 18 bursts. Note that among these 18 bursts, only GRB 210510806 lacks a measured  $E_p$ . Following Paul (2018a,b), we randomly sample this burst’s  $E_p$  from the observed  $E_p$  distribution of *Fermi* sGRBs with spectral measurements. To validate our pseudo-redshift estimates, we compare the cumulative distributions of measured (blue line) and pseudo-redshifts (orange line) in Figure 3 and perform a Kolmogorov-Smirnov (K-S) test between these distributions. The K-S test statistic,  $P_{\text{KS}}$ , quantifies

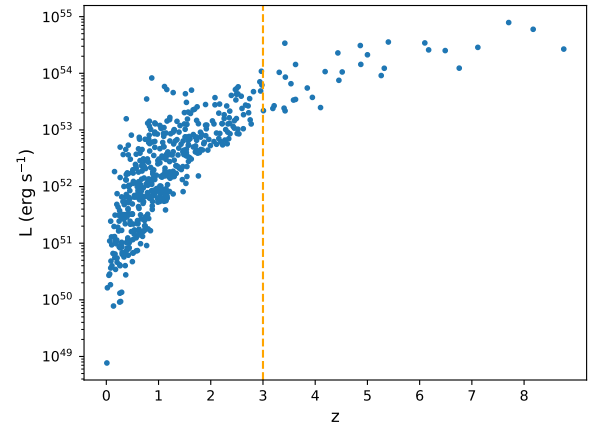


**Figure 2.** Pseudo redshift–luminosity distribution of 512 *Fermi* sGRBs estimated by the  $E_p$ – $L$  correlation. The vertical dashed line represents the truncated redshift of  $z = 3$ , below which 478 bursts are used for our analysis.

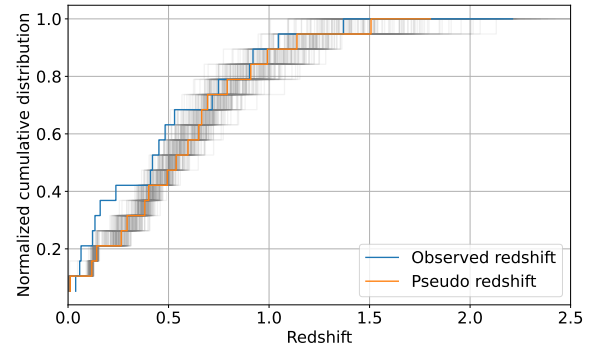


**Figure 3.** Normalized cumulative redshift distribution for 18 sGRBs with known redshifts in our sample (blue line). The orange line represents the pseudo-redshift distribution for these bursts derived from the  $E_p$ – $L$  correlation. The gray lines show uncertainty regions estimated from 100 Monte Carlo simulations.

the likelihood that two datasets are drawn from the same distribution: a higher  $P_{\text{KS}}$ -value indicates greater consistency between the distributions. By convention,  $P_{\text{KS}} > 0.05$  is considered insufficient evidence to reject the null hypothesis, while of  $P_{\text{KS}} < 10^{-4}$  provides strong evidence against the null hypothesis (i.e., the distributions differ). The resulting  $P_{\text{KS}}$ -value of 0.80 indicates that we cannot reject the null hypothesis. Moreover, we estimate an uncertainty region for the pseudo-redshift distribution of these 18 bursts. Redshift errors primarily originate from  $E_p$  uncertainties, so we performed 100 Monte Carlo simulations per data point to derive cumulative distributions. Gray lines in Figure 3 show these results, indicating the uncertainty region partially covers the observed distribution (blue line). Therefore, we conclude that the redshift distribution estimated from the  $E_p$ – $L$  correlation is broadly consistent with the observed distribution, supporting the use of  $E_p$ – $L$  correlation as a statistically valid distance indicator for sGRBs. Notably, Paul (2018a) demonstrated that random  $E_p$  sampling statistically replicates the redshift distribution of long GRBs. Figure 3 confirms this approach also works for sGRBs: their redshift distribution is replicated through  $E_p$  uncertainty propagation and random  $E_p$  draws for spectrally unmeasured bursts.

In our pseudo-redshift estimation, we make no assertion regarding the accuracy of individual values. We do not assess pseudo-redshift accuracy per GRB, as our analysis relies exclusively on statistical

**Table 1.** The measured redshifts and pseudo-redshift estimates of 18 sGRBs.

GRB Name	Measured Redshift <sup>a</sup>	Pseudo Redshift <sup>b</sup>
GRB 090927422	1.37	0.66
GRB 100625773	0.45	0.66
GRB 200826187	0.75	0.25
GRB 090510016	0.90	1.14
GRB 080905499	0.12	1.82
GRB 231024556	0.06	0.40
GRB 150101641	0.13	0.26
GRB 131004904	0.72	0.79
GRB 100117879	0.92	1.01
GRB 100206563	0.41	0.55
GRB 111117510	2.21	0.69
GRB 210323918	0.42	0.91
GRB 160624477	0.48	1.55
GRB 100216422	0.04	0.28
GRB 220211047	0.53	0.36
GRB 201221963	1.05	0.91
GRB 210510806	0.22	1.11 <sup>c</sup>
GRB 160821937	0.16	0.59

*Note.* <sup>a</sup>The measured redshifts are obtained from [https://user-web.icecube.wisc.edu/~grbweb\\_public/Summary\\_table.html](https://user-web.icecube.wisc.edu/~grbweb_public/Summary_table.html). <sup>b</sup>Pseudo-redshift estimation involves statistical analysis, and measured versus pseudo redshifts are not meant to be equal since pseudo redshifts derive from the empirical  $E_p$ - $L$  correlation and, for bursts without spectral measurements, random  $E_p$  sampling. <sup>c</sup>For GRB 210510806, its reported pseudo redshift corresponds to a single random  $E_p$  draw.

distribution comparisons. This approach assigns pseudo redshifts to bursts in a collective statistical context only. Nevertheless, this limitation does not invalidate our methodology, since we use pseudo-redshifts and derived luminosities solely as ensemble quantities for modeling the sGRB LF and formation rate.

### 3 SGRB LUMINOSITY FUNCTION AND FORMATION RATE

#### 3.1 Analysis method

In this work, we use the maximum likelihood method proposed by Marshall et al. (1983) to constrain the sGRB LF and redshift distribution. The likelihood function is defined as (e.g., Chiang & Mukherjee 1998; Narumoto & Totani 2006; Ajello et al. 2009, 2012; Abdo et al. 2010; Lan et al. 2019, 2021, 2022)

$$\mathcal{L} = \exp(-N_{\text{exp}}) \prod_{i=1}^{N_{\text{obs}}} \Phi(L_i, z_i, t_i), \quad (3)$$

where  $N_{\text{exp}}$  is the expected number of sGRB detections,  $N_{\text{obs}}$  is the observed number of the sample, and  $\Phi(L, z, t)$  denotes the observed rate of sGRBs per unit time at redshift  $z \sim z + dz$  with luminosity

$L \sim L + dL$ , which can be written as

$$\Phi(L, z, t) = \frac{d^3 N}{dt dL dz} = f_{\text{sky}} f_{\text{not\_SAA}} \frac{R_{\text{sGRB}}(z)}{1+z} \frac{dV(z)}{dz} \phi(L), \quad (4)$$

where  $f_{\text{sky}} = 0.7$  is the sky-coverage fraction of *Fermi*/GBM,<sup>2</sup>  $f_{\text{not\_SAA}} = 0.85$  denotes the fraction of *Fermi*'s orbit outside the South Atlantic Anomaly (SAA),  $R_{\text{sGRB}}(z)$  is the comoving rate density of sGRBs in units of  $\text{Gpc}^{-3} \text{yr}^{-1}$ , the factor  $(1+z)^{-1}$  reflects the cosmological time dilation,  $\phi(L)$  is the normalized LF of sGRBs, and  $dV(z)/dz = 4\pi c d_l^2(z)/[H_0(1+z)^2 \sqrt{\Omega_m(1+z)^3 + \Omega_\Lambda}]$  is the comoving volume element in a flat  $\Lambda$ CDM cosmology.

It is believed that sGRBs originate from the mergers of two compact stars, either NS-NS or NS-BH. A compact binary system undergoes a long inspiral phase before the final merger, resulting in a significant time delay with respect to star formation (Faber & Rasio 2012; Burns 2020). If we assume that the fraction of mass forming compact binary systems relative to the total mass forming newborn stars remains constant over cosmological time, then the sGRB rate density  $R_{\text{sGRB}}(z)$  can be represented as a convolution of the star formation rate density (SFRD)  $\psi_\star(z)$  and the probability density function of the delay time distribution  $P(\tau)$  (Paul 2018b; Liu & Yu 2019; Luo et al. 2022):

$$R_{\text{sGRB}}(z) = f_b C \int_{\tau_{\text{min}}}^{\tau_{\text{max}}} \psi_\star[z'(\tau)] P(\tau) d\tau, \quad (5)$$

where  $f_b = (1 - \cos \theta_j)$  represents the beaming factor for a top-hat jet with opening angle  $\theta_j$ , and  $C$  is the sGRB formation efficiency per unit available mass (in units of  $\text{M}_\odot^{-1}$ ). In the maximum likelihood analysis, the parameters  $C$  and  $f_b$  are degenerate. That is, one can vary either  $C$  or  $f_b$ , but not both. Therefore, we adopt a definition

$$\eta \equiv f_b C, \quad (6)$$

where  $\eta$  is the ' $f_b$ -free' formation efficiency, still in units of  $\text{M}_\odot^{-1}$ . Here,  $z'(\tau)$  denotes the redshift at the formation of the compact binary system, while  $z$  corresponds to the redshift of the sGRB event. Thus, the delay time between the formation and merger of the compact binary system is given by  $\tau = t(z) - t(z')$ , where  $t(z)$  and  $t(z')$  are the ages of the Universe at redshifts  $z$  and  $z'$ , respectively. In view of the fact that the progenitors of NSs usually have initial masses of  $10\text{--}29 \text{ M}_\odot$ , and their lifetimes are  $10\text{--}30 \text{ Myr}$ , we set the minimum delay time to be  $\tau_{\text{min}} = 10 \text{ Myr}$ , as done by Luo et al. (2022) in their treatment. The age of the Universe at redshift  $z$ ,  $t(z)$ , is set as the maximum delay time  $\tau_{\text{max}}$ . The SFRD  $\psi_\star(z)$  can be expressed approximately by the analytical form (Yüksel et al. 2008):

$$\psi_\star(z) = \rho_0 \left[ (1+z)^{3.4\omega} + \left( \frac{1+z}{5000} \right)^{-0.3\omega} + \left( \frac{1+z}{9} \right)^{-3.5\omega} \right]^{1/\omega}, \quad (7)$$

where  $\rho_0 = 0.02 \text{ M}_\odot \text{ Mpc}^{-3} \text{ yr}^{-1}$  is the local SFRD, and  $\omega = -10$ .

For the delay time distribution  $P(\tau)$ , we consider three most widely discussed models: Gaussian, Lognormal, and Power law, whose functional forms can be expressed as:

(i) Gaussian (Virgili et al. 2011):

$$P(\tau) \propto \frac{1}{\sqrt{2\pi}\sigma_G} \exp \left[ -\frac{(\tau - t_G)^2}{2\sigma_G^2} \right], \quad (8)$$

<sup>2</sup> *Fermi* is a low earth-orbit satellite that suffers from limited sky coverage because the Earth blocks  $\sim 30\%$  of the sky.

where  $t_G$  and  $\sigma_G$  represent, respectively, the mean and the standard deviation of  $\tau$ .

(ii) Lognormal (Wanderman & Piran 2015):

$$P(\tau) \propto \frac{1}{\sqrt{2\pi}\sigma_{LN}} \exp \left[ -\frac{(\ln \tau - \ln t_{LN})^2}{2\sigma_{LN}^2} \right], \quad (9)$$

where  $\ln t_{LN}$  and  $\sigma_{LN}$  represent, respectively, the mean and the standard deviation of  $\ln \tau$ .

(iii) Power law (Nakar et al. 2006b):

$$P(\tau) \propto \tau^{-\gamma}, \quad (10)$$

where  $\gamma$  is the power-law index.

For the sGRB LF  $\phi(L)$ , we adopt the widely recognized expression in terms of a broken power law:

$$\phi(L) \propto \begin{cases} \left(\frac{L}{L_b}\right)^{-\nu_1}; & L \leq L_b, \\ \left(\frac{L}{L_b}\right)^{-\nu_2}; & L > L_b, \end{cases} \quad (11)$$

where  $\nu_1$  and  $\nu_2$  are the power-law indices before and after the break luminosity  $L_b$ . The normalization constant of the LF is calculated between the minimum and maximum luminosities,  $L_{\min} = 10^{49} \text{ erg s}^{-1}$  and  $L_{\max} = 10^{55} \text{ erg s}^{-1}$  (Tan et al. 2018).

Finally, when considering *Fermi*/GBM having a flux threshold of  $P_{\lim} = 4.1 \text{ photons cm}^{-2} \text{ s}^{-1}$  in the 10–1000 keV energy band, the expected number of sGRBs should be

$$N_{\exp} = T f_{\text{sky}} f_{\text{not-SAA}} \int_0^{z_{\max}} \frac{R_{\text{sGRB}}(z)}{1+z} \frac{dV(z)}{dz} dz \int_{\max[L_{\min}, L_{\lim}(z)]}^{L_{\max}} \phi(L) dL, \quad (12)$$

where  $T \sim 15.5 \text{ yr}$  is the observational period of *Fermi* that covers our sample, and  $z_{\max} = 3$  corresponds to the maximum redshift of our sample. For a given redshift  $z$ , the luminosity threshold can be determined by

$$L_{\lim}(z) = 4\pi d_L^2(z) P_{\lim} k(z), \quad (13)$$

where  $k(z)$  is the spectral  $k$ -correction factor converting *Fermi*/GBM's observed energy band of 10–1000 keV (denoted by  $E_{\min}$ – $E_{\max}$  keV) into the source-frame band of 1– $10^5$  keV. For *Fermi* bursts, the flux threshold  $P_{\lim}$  is given in units of photons  $\text{cm}^{-2} \text{ s}^{-1}$ , hence

$$k(z) = \frac{\int_{1/(1+z) \text{ keV}}^{10^5/(1+z) \text{ keV}} EN(E) dE}{\int_{E_{\min}}^{E_{\max}} N(E) dE}, \quad (14)$$

where  $N(E)$  is the observed photon spectrum. While for other detectors with  $P_{\lim}$  given in  $\text{erg cm}^{-2} \text{ s}^{-1}$ , the  $k$ -correction factor should be rewritten as follows:

$$k(z) = \frac{\int_{1/(1+z) \text{ keV}}^{10^5/(1+z) \text{ keV}} EN(E) dE}{\int_{E_{\min}}^{E_{\max}} EN(E) dE}. \quad (15)$$

To describe  $N(E)$ , we adopt a typical Band spectrum, characterized by photon spectral indices of  $\alpha = -1$  and  $\beta = -2.25$  (Band et al. 1993; Preece et al. 2000; Kaneko et al. 2006). For a given  $L$ , the observer-frame spectral peak energy  $E_p$  is estimated through the empirical  $E_p$ – $L$  correlation (i.e., Equation 1).

### 3.2 Results

For a given delay-time distribution model, we optimize the free parameters by maximizing the likelihood function (Equation 3). The delay time distribution  $P(\tau)$  has one or two free parameters (e.g.,  $t_G$  and  $\sigma_G$  for Gaussian delay,  $t_{LN}$  and  $\sigma_{LN}$  for lognormal delay, or  $\gamma$  for power-law delay). The sGRB LF  $\phi(L)$  has three free parameters ( $\nu_1$ ,  $\nu_2$ , and  $L_b$ ). Additionally, the sGRB rate density  $R_{\text{sGRB}}(z)$ , given by Equation (5), depends on the sGRB formation efficiency  $\eta$ , resulting in a total of five or six free parameters. For each model, the Python Markov chain Monte Carlo (MCMC) module, EMCEE (Foreman-Mackey et al. 2013), is employed to derive multidimensional parameter constraints from the observational data. The one-dimensional (1D) probability distributions and two-dimensional (2D) confidence regions (with  $1-2\sigma$  contours) for the parameters of different delay-time distribution models are shown in Figures A1–A3. These plots demonstrate that the sGRB formation efficiency ( $\eta$ ) and the parameters of the sGRB LF ( $\nu_1$ ,  $\nu_2$ , and  $L_b$ ) are well constrained, regardless of the assumed delay-time distribution. For the power-law delay model, the power-law index ( $\gamma$ ) is also well determined. In contrast, for the Gaussian and lognormal delay models, there is a strong degeneracy between the delay parameters:  $t_G$  and  $\sigma_G$  for the Gaussian model, and  $t_{LN}$  and  $\sigma_{LN}$  for the lognormal model. This degeneracy allows only an upper limit to be placed on  $\sigma_G$  (Gaussian) or  $\sigma_{LN}$  (lognormal).

Table 2 lists the best-fit parameters and their corresponding  $1\sigma$  uncertainties for different models. In the last two columns, we also list the logarithmic likelihood value ( $\ln \mathcal{L}$ ) and the Deviance Information Criterion (DIC) score, which can be used to statistically judge which of the models is preferred by the observational data. For each model, the DIC score is calculated as  $\text{DIC} = \overline{D(\theta)} + p_D$ , where  $\overline{D(\theta)} = -2 \ln \mathcal{L}(\theta)$  is the deviance of the likelihood, and  $p_D = \overline{D(\theta)} - D(\bar{\theta})$ . Here,  $D(\theta)$  represents the mean deviance averaged over posterior samples,  $\bar{\theta}$  denotes the posterior mean of the parameters. Unlike the Akaike and Bayesian Information Criteria, the DIC explicitly accounts for scenarios where parameters (or combinations of parameters) are poorly constrained by observational data, a common challenge in astrophysics (Liddle 2007). Given multiple different models  $\mathcal{M}_1, \mathcal{M}_2, \dots, \mathcal{M}_N$ , each with the corresponding DIC scores  $\text{DIC}_1, \text{DIC}_2, \dots, \text{DIC}_N$ , the unnormalized confidence that model  $\mathcal{M}_i$  is correct is the Akaike weight  $\exp(-\text{DIC}_i/2)$ . Thus, the relative probability that  $\mathcal{M}_i$  is statistically preferred is

$$P(\mathcal{M}_i) = \frac{\exp(-\text{DIC}_i/2)}{\exp(-\text{DIC}_1/2) + \dots + \exp(-\text{DIC}_N/2)}. \quad (16)$$

Figure 4 presents the redshift and luminosity distributions of 478 sGRBs with  $P \geq 4.1 \text{ photons cm}^{-2} \text{ s}^{-1}$  and  $z \leq 3$ . To facilitate a direct comparison among different delay-time distribution models, we show in Figure 4 the best-fit theoretical curves for the power-law delay model (yellow solid), the Gaussian delay model (blue dashed), and the lognormal delay model (purple dot-dashed). One can see from this plot that the expectations from these three models appear to fit the observed  $z$  and  $L$  distributions comparably well. According to the DIC model selection criterion, we find that the Gaussian delay model is statistically preferred with an approximate relative probability of 99.99%.

With the best-fit parameters presented in Table 2, we are able to calculate the local sGRB formation rate at  $z = 0$ ,  $R_{\text{sGRB}}(0)$ , using Equation (5). We find  $R_{\text{sGRB}}(0) = 1.37_{-0.27}^{+0.30} \text{ Gpc}^{-3} \text{ yr}^{-1}$  for the Gaussian delay model,  $1.63_{-0.27}^{+0.44} \text{ Gpc}^{-3} \text{ yr}^{-1}$  for the lognormal delay model, and  $1.78_{-0.17}^{+0.12} \text{ Gpc}^{-3} \text{ yr}^{-1}$  for the power-law delay model, which are consistent with each other within the  $1\sigma$  confidence level

**Table 2.** Best-fitting parameters for different delay-time distribution models.

Delay model	Delay parameter	$\log_{10} \eta$ ( $M_{\odot}^{-1}$ )	$\log_{10} L_b$ ( $\text{erg s}^{-1}$ )	$\nu_1$	$\nu_2$	$\ln \mathcal{L}$	DIC
Gaussian	$t_G = 1.14^{+0.02}_{-0.17}$ , $\sigma_G < 0.26$	$1.45^{+0.12}_{-0.08}$	$53.25^{+0.13}_{-0.18}$	$1.40^{+0.04}_{-0.04}$	$2.76^{+0.64}_{-0.35}$	-47486	94996
Lognormal	$t_{LN} = 2.14^{+0.01}_{-0.28}$ , $\sigma_{LN} < 0.06$	$1.30^{+0.06}_{-0.06}$	$53.22^{+0.16}_{-0.10}$	$1.37^{+0.03}_{-0.03}$	$2.72^{+0.51}_{-0.28}$	-47520	95053
Power law	$\gamma = 2.04^{+0.44}_{-0.48}$	$1.51^{+0.06}_{-0.06}$	$53.17^{+0.10}_{-0.09}$	$1.29^{+0.04}_{-0.04}$	$2.63^{+0.24}_{-0.30}$	-47526	95058

Note.  $t_G$ ,  $t_{LN}$ , and  $\sigma_G$  are in units of Gyr, and  $\sigma_{LN}$  is in units of ln Gyr.

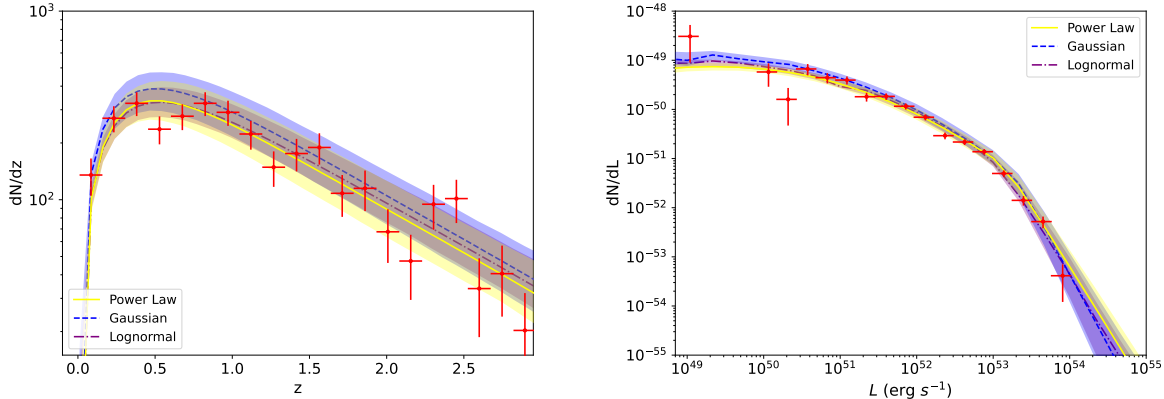


**Figure 4.** Redshift and luminosity distributions of 478 *Fermi* sGRBs with  $P \geq 4.1 \text{ photons cm}^{-2} \text{ s}^{-1}$  and  $z \leq 3$  (the red points, with the detection number in each redshift or luminosity bin, are indicated by a solid point with Poisson error bars). Different curves correspond to the expected distributions from various best-fit delay time distribution models: power-law delay (yellow solid lines), Gaussian delay (blue dashed lines), and lognormal delay (purple dot-dashed lines). Shaded areas show the  $1\sigma$  confidence regions of the corresponding models.

$1\sigma$ . We would like to stress that our derived local sGRB formation rate is broadly consistent with previous results (Guetta & Piran 2005; Yonetoku et al. 2014; Ghirlanda et al. 2016; Paul 2018b). The event rate of BNS mergers is estimated to be as high as  $R_{\text{BNS}} = 320^{+490}_{-240} \text{ Gpc}^{-3} \text{ yr}^{-1}$ , as inferred from the second LIGO-Virgo GW transient catalog (Abbott et al. 2021). The discrepancy between the local sGRB formation rate and BNS merger rate arises primarily from the high collimation of GRB jets. For top-hat jets, the beaming factor is calculated as  $f_b = R_{\text{sGRB}}(0)/R_{\text{BNS}}$ , yielding a half-opening angle of  $\theta_j \sim 3^\circ - 12^\circ$ . This range is in good agreement with previous estimates of  $\theta_j \sim 3^\circ - 26^\circ$  (Fong et al. 2013, 2015; Margutti et al. 2012).

In our research, the inferred sGRB LF exponents  $\nu_1$  and  $\nu_2$  range from 1.25 to 1.44 and 2.33 to 3.40, respectively, at the  $1\sigma$  confidence level. We emphasize that if the LF is defined in terms of  $\phi(L)dL$  rather than  $\phi(L)d \log L$ , our derived LF exponents are roughly consistent with previous studies:  $\nu_1 = 1.6 \pm 0.4$  and  $\nu_2 = 3.0 \pm 1.0$  by Guetta & Piran (2006),  $\nu_1 = 1.95^{+0.12}_{-0.12}$  and  $\nu_2 = 3.0^{+1.0}_{-0.8}$  by Wanderman & Piran (2015), and  $\nu_1 = 1.29 \pm 0.01$  and  $\nu_2 = 2.07 \pm 0.01$  by Zhang & Wang (2018).

#### 4 JOINT GW AND SGRB DETECTION

In this section, we will first describe the synthetic BNS population and provide estimates of the GW detection rates by the GW detector networks. Next, we will calculate the sGRB detection rates for high-energy satellites. Finally, we will study the joint detection prospects of GWs and their sGRB counterparts from BNS mergers.

#### 4.1 GW detection rate simulation

Following Bhattacharjee et al. (2024), we inject  $N_{\text{inj}} = 300,000$  sources from BNS mergers up to a luminosity distance of  $d_L = 1.6 \text{ Gpc}$  (corresponding to a comoving distance of  $\sim 1.2 \text{ Gpc}$  and redshift  $z \sim 0.3$ ). The number of injected sources is oversampled by a factor of  $\sim 130$  compared to the merger rate of BNSs within the same comoving volume, based on the median BNS merger event rate of  $320 \text{ Gpc}^{-3} \text{ yr}^{-1}$  (Abbott et al. 2021). This oversampling is conducted to avoid any effects of small number statistic on our results. The injected sources are uniformly distributed in the rest-frame comoving volume, which translates to a redshift probability distribution of

$$\frac{dp(z)}{dz} \propto \frac{1}{1+z} \frac{dV(z)}{dz}. \quad (17)$$

We assume that the mass distribution of the NSs obeys a normal distribution with a mean of  $1.33 M_{\odot}$  and a standard deviation of  $0.09 M_{\odot}$  (Özel & Freire 2016). The spins of the NSs are uniformly distributed between  $0 < \chi < 0.05$ , with the upper limit set by the maximum known NS spin (Zhu et al. 2018). The direction of the orbital angular momentum is uniformly distributed in space. We generate the GW waveforms using the Python package PyCBC<sup>3</sup> with the IMPRPhenomPv2 approximant model (Schmidt et al. 2012; Hannam et al. 2014; Khan et al. 2016).

To determine which injected BNS merger events can be detected by two different GW detection networks, IGWN4 and IGWN5, we

<sup>3</sup> <https://pycbc.org/>

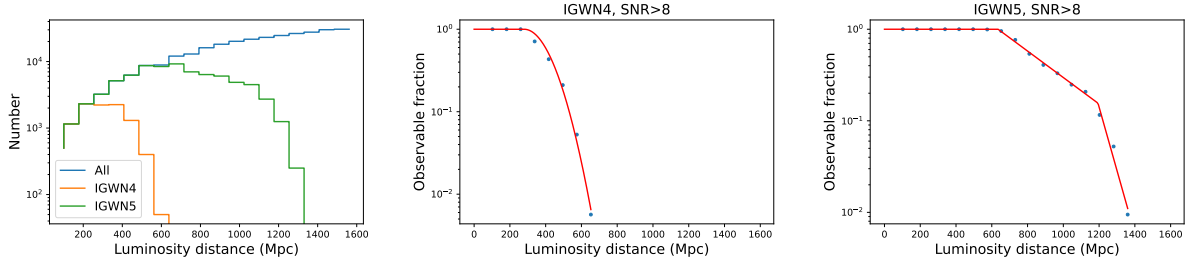


**Figure 5.** Left panel: Luminosity distance distribution of injected BNS merger events (blue histogram). The yellow and green histograms correspond to the distributions of events detected above the threshold  $\text{SNR}_{\text{net}}$  of 8 by IGWN4 and IGWN5, respectively. Middle panel: GW detection rate  $R_{\text{GW}}(z)$  as a function of luminosity distance, calculated as the ratio of IGWN4 detections to the total injected events at each redshift. The best-fit curve is described by Equation (20). Right panel: Same as the middle panel but for IGWN5, with the best-fit curve parametrized by Equation (21).

consider those events above a particular threshold value of the net-work signal-to-noise ratio, i.e.,

$$\text{SNR}_{\text{net}} = \sqrt{\sum_{\text{det}} \text{SNR}_{\text{det}}^2}, \quad (18)$$

where  $\text{SNR}_{\text{det}}$  is the signal-to-noise ratio (SNR) of a single detector (Pai et al. 2001). In this work, we define the criterion of  $\text{SNR}_{\text{net}} > 8$  as the detection threshold (Petrov et al. 2022). For a given single detector, the  $\text{SNR}_{\text{det}}$  could be calculated by (Babak et al. 2021)

$$\text{SNR}_{\text{det}}^2 = 4 \text{Re} \left( \int_{f_{\text{min}}}^{f_{\text{max}}} df \frac{\tilde{X} \tilde{X}^*}{S_n(f)} \right), \quad (19)$$

where  $\tilde{X}$  represents the complex GW signal, and  $S_n(f)$  is the noise power spectral density of the corresponding detector, which can be downloaded from the Sensitive Curves website<sup>4</sup>.

From the above simulation, we obtain the distribution of the injected BNS merger events over luminosity distance  $d_l(z)$ , which is presented in the left panel of Figure 5 as the blue histogram. In this plot, we also show the distribution of the events detected above the threshold  $\text{SNR}_{\text{net}}$  of 8 by either IGWN4 (yellow histogram) or IGWN5 (green histogram). The middle (right) panel of Figure 5 displays the GW detection rate  $R_{\text{GW}}(z)$  as a function of redshift (or  $d_l$ ), calculated by dividing the number of detections from IGWN4 (IGWN5) by the total injected events at each redshift. Here, we model  $R_{\text{GW}}(z)$  with empirical piecewise functions. For the case of IGWN4, we have

$$\log_{10} R_{\text{GW}}(z) = \begin{cases} 0; & d_l(z) \leq d_b, \\ \kappa [d_l(z) - d_b]^2 + \xi [d_l(z) - d_b]; & d_l(z) > d_b, \end{cases} \quad (20)$$

with best-fit parameters  $d_b = 280 \text{ Mpc}$ ,  $\kappa = -1.56 \times 10^{-5}$ , and  $\xi = 4.04 \times 10^{-8}$ . For IGWN5, a triple power-law parametrizes  $\log_{10} R_{\text{GW}}(d_l)$ :

$$\log_{10} R_{\text{GW}}(z) = \begin{cases} 0; & d_l(z) \leq d_{b_1}, \\ \kappa [d_l(z) - d_{b_1}]; & d_{b_1} < d_l(z) \leq d_{b_2}, \\ \kappa [d_l(z) - d_{b_1}] + \xi [d_l(z) - d_{b_2}]; & d_l(z) > d_{b_2}, \end{cases} \quad (21)$$

with best-fit parameters  $d_{b_1} = 635 \text{ Mpc}$ ,  $d_{b_2} = 1193 \text{ Mpc}$ ,  $\kappa = -1.44 \times 10^{-3}$ , and  $\xi = -6.92 \times 10^{-3}$ .

<sup>4</sup> <https://git.ligo.org/sensitivity-curves/observing-scenario-paper-2019-2020-update/-/tree/master>

## 4.2 sGRB detection rates

To determine the prospects of sGRB detection, we consider three existing high-energy GRB detectors: *Fermi*/GBM (10–1000 keV), the Gamma-Ray Monitor (GRM) of *SVOM* (1–1000 keV), and the Wide-field X-ray Telescope (WXT) of *EP* (0.5–4 keV). The energy bands, flux thresholds, sky-coverage fractions, and SAA-outage fractions of these three high-energy emissions are summarized in Table 3.

With the flux threshold and effective detection fraction for each detector, we compute the sGRB detection rate per year up to a luminosity distance of  $d_L = 1.6 \text{ Gpc}$  (corresponding to  $z = 0.3$ ), consistent with the distance limit applied to BNS merger events. The calculation employs Equation (12), with model-free parameters fixed to the values in Table 2. For the Gaussian delay model, our results show that the sGRB detection rate is  $3.28^{+0.48}_{-0.58} \text{ yr}^{-1}$  for *Fermi*/GBM,  $2.69^{+0.32}_{-0.40} \text{ yr}^{-1}$  for *SVOM*/GRM, and  $0.78^{+0.09}_{-0.11} \text{ yr}^{-1}$  for *EP*/WXT. For the same detector, similar sGRB detection rates are derived for different delay-time distribution models. The derived sGRB detection rates for the high-energy GRB detectors are listed in Columns 2–4 of Table 4. It is clear that *Fermi*/GBM has the highest sGRB detection rate. Due to their relatively low sky coverage, the other two detectors, *SVOM*/GRM and *EP*/WXT, have lower detection rates, in that order.

It should be underlined that our analysis is limited by the distance cut-off of  $d_L = 1.6 \text{ Gpc}$  ( $z = 0.3$ ). Thus, events beyond this distance limit are missed by our calculations. However, in reality, many higher-redshift ( $z > 0.3$ ) events will be detected by high-energy GRB missions. This makes the sGRB detection rates calculated here lower than the true sGRB detection rates by these missions.

Our final *Fermi*/GBM sample contains 478 sGRBs with peak photon flux  $P \geq 4.1 \text{ photons cm}^{-2} \text{ s}^{-1}$  and redshift  $z \leq 3$ . Over the 15.5 yr mission period, the observed *Fermi*/GBM detection rate is  $\sim 30.8 \text{ yr}^{-1}$ . Assuming a *Fermi*/GBM flux threshold of 4.1 photons  $\text{cm}^{-2} \text{ s}^{-1}$  in the 10–1000 keV energy range, we predict a detectable sGRB rate at  $z \leq 3$  of  $34.7^{+8.0}_{-5.8} \text{ yr}^{-1}$  (Gaussian delay model),  $30.1^{+3.8}_{-3.4} \text{ yr}^{-1}$  (Lognormal delay model), and  $29.3^{+9.7}_{-8.7} \text{ yr}^{-1}$  (power-law delay model) using Equation (12). These predictions agree well with the observed detection rate ( $\sim 30.8 \text{ yr}^{-1}$ ) within uncertainties.

## 4.3 Joint sGRB and GW detection rates

By combining the GW detection rate  $R_{\text{GW}}(z)$  with the observed sGRB distributions, the expected number of joint sGRB and GW detections from BNS mergers can be estimated using specific GRB

**Table 3.** The energy bands, flux thresholds, Sky-coverage fractions, and SAA-outage fractions of the high-energy emissions.

Mission	Energy band (keV)	Flux threshold	Sky-coverage fraction	SAA-outage fraction
			$(f_{\text{sky}})$	$(f_{\text{not\_SAA}})$
<i>Fermi</i> /GBM	10–1000	4.1 (photons $\text{cm}^{-2} \text{s}^{-1}$ )	0.7	0.85
<i>SVOM</i> /GRM <sup>(a)</sup>	1–1000	3.2 (photons $\text{cm}^{-2} \text{s}^{-1}$ )	0.24	0.85
<i>EP</i> /WXT <sup>(b)</sup>	0.5–4	$8.9 \times 10^{-10}$ (erg $\text{cm}^{-2} \text{s}^{-1}$ )	0.09	0.67

Note. (a) [Wei et al. \(2016\)](#), (b) [Yuan et al. \(2015\)](#).

**Table 4.** The sGRB and joint sGRB + GW detection rates for all combinations of high-energy GRB missions, GW networks, and delay-time distribution models. Columns 2–4 give the sGRB detection rates for the three GRB missions, independent of GW detection. Note that these rates are estimated for events with  $d_L < 1.6 \text{ Gpc}$  (corresponding to  $z < 0.3$ ), which is the distance limit of this work; they should not be confused with the total sGRB detection rates (see the discussion at the end of section 4.2). The last six columns provide the joint sGRB + GW detection rates. For instance, the last cell of this table states that for the Gaussian delay model, *EP*/WXT + IGWN5 will detect  $0.24^{+0.03}_{-0.04}$  events per year. All the results are presented at the  $1\sigma$  confidence level.

Delay model	sGRB detection rate ( $\text{yr}^{-1}$ )			IGWN4 joint detection rate ( $\text{yr}^{-1}$ )			IGWN5 joint detection rate ( $\text{yr}^{-1}$ )		
	<i>Fermi</i> /GBM	<i>SVOM</i> /GRM	<i>EP</i> /WXT	<i>Fermi</i> /GBM	<i>SVOM</i> /GRM	<i>EP</i> /WXT	<i>Fermi</i> /GBM	<i>SVOM</i> /GRM	<i>EP</i> /WXT
Gaussian	$3.28^{+0.48}_{-0.58}$	$2.69^{+0.32}_{-0.40}$	$0.78^{+0.09}_{-0.11}$	$0.24^{+0.03}_{-0.03}$	$0.09^{+0.01}_{-0.01}$	$0.02^{+0.01}_{-0.01}$	$1.18^{+0.17}_{-0.21}$	$0.69^{+0.10}_{-0.12}$	$0.24^{+0.03}_{-0.04}$
Lognormal	$2.82^{+0.22}_{-0.31}$	$2.06^{+0.16}_{-0.22}$	$0.76^{+0.08}_{-0.06}$	$0.21^{+0.03}_{-0.02}$	$0.08^{+0.01}_{-0.01}$	$0.02^{+0.01}_{-0.01}$	$1.03^{+0.19}_{-0.10}$	$0.59^{+0.10}_{-0.06}$	$0.21^{+0.01}_{-0.02}$
Power law	$3.19^{+0.31}_{-0.35}$	$1.99^{+0.28}_{-0.25}$	$0.57^{+0.08}_{-0.07}$	$0.21^{+0.02}_{-0.02}$	$0.08^{+0.01}_{-0.01}$	$0.02^{+0.01}_{-0.01}$	$1.12^{+0.14}_{-0.11}$	$0.57^{+0.06}_{-0.06}$	$0.16^{+0.01}_{-0.01}$

and GW facilities through the following equation:

$$N_{\text{joint}} = T f_{\text{sky}} f_{\text{not\_SAA}} \int_0^{z_{\text{lim}}} \frac{R_{\text{sGRB}}(z) R_{\text{GW}}(z)}{1+z} \frac{dV(z)}{dz} dz \int_{\max[L_{\text{min}}, L_{\text{lim}}(z)]}^{L_{\text{max}}} \phi(L) dL, \quad (22)$$

where  $z_{\text{lim}} = 0.3$  (corresponding to  $1.6 \text{ Gpc}$ ) is the distance limit of this work. It is important to note that in the calculations above (specifically Equations 12 and 22), all sGRB observations are assumed to be on-axis, with jets modeled under a top-hat structure. However, observations of GW170817 and GRB 170817A suggest that GRB jets likely follow a wide angular distribution (Abbott et al. 2017). Because the luminosity of a given sGRB decreases rapidly as the viewing angle  $\theta$  relative to its symmetry axis increases, off-axis detection is feasible only for nearby sources. Consequently, the top-hat assumption remains a reasonable approximation for sGRBs at cosmological distances. For nearby events like GRB 170817A, however, the jet structure and the potential for off-axis detection become significant.

Because of the on-axis assumption, the sGRB LF  $\phi(L)$  derived in Section 3 describes only the distribution of the core luminosity  $L$  of GRB jets. For a structured jet, the observed luminosity is expressed as

$$L_{\text{obs}}(\theta) = L J(\theta), \quad (23)$$

where  $J(\theta)$  is a function describing the viewing-angle  $\theta$  dependence of the luminosity, and  $L$  is the on-axis luminosity at  $\theta = 0$ . The observed LF must instead be expressed as

$$\phi'(L_{\text{obs}}) \propto \int_0^{\pi/2} \phi[L_{\text{obs}}/J(\theta)] \sin\theta d\theta. \quad (24)$$

To account for structured jets, the expected number of joint sGRB and GW detections from BNS mergers is calculated by

$$N_{\text{joint}} = T f_{\text{sky}} f_{\text{not\_SAA}} \int_0^{z_{\text{lim}}} \frac{R_{\text{sGRB}}(z) R_{\text{GW}}(z)}{1+z} \frac{dV(z)}{dz} dz \int_{\max[L_{\text{min}}, L_{\text{lim}}(z)]}^{L_{\text{max}}} \phi'(L_{\text{obs}}) dL_{\text{obs}}. \quad (25)$$

Following Liu & Yu (2019), we adopt a Gaussian jet model  $J(\theta) = e^{-(\frac{\theta}{2\theta_c})^2}$ , where  $\theta_c = 3^\circ$  defines the angular core width. Again, in our calculations, the model-free parameters are fixed at the best-fit values given in Table 2. The joint detection rate is calculated using Equation (25) with  $T = 1 \text{ yr}$ .

For the sensitivity of the IGWN4, the overall joint sGRB and GW detection rates are rather low. The joint detection rates for the high-energy GRB detectors *Fermi*/GBM, *SVOM*/GRM, and *EP*/WXT lie in the range of  $0.19$ – $0.27$ ,  $0.07$ – $0.10$ , and  $0.01$ – $0.03 \text{ yr}^{-1}$ , respectively, for different delay-time distribution models (see Columns 5–7 of Table 4). The joint detection rate expected from *Fermi*/GBM and IGWN4 means that only 1–3 sGRB and GW associated events would be detected in about 10 years of observation, which is consistent with the current result that only one joint detection of GW170817/GRB 170817A has been found. After the GW detection network is upgraded to IGWN5, the joint detection rates increase to  $0.93$ – $1.35$ ,  $0.51$ – $0.79$ , and  $0.15$ – $0.27 \text{ yr}^{-1}$  for *Fermi*/GBM, *SVOM*/GRM, and *EP*/WXT, respectively (see Columns 8–10 of Table 4).

Our joint sGRB and GW detection rates align well with those estimated in previous studies. For instance, Colombo et al. (2022) reported a joint detection rate of  $\sim 0.17 \text{ yr}^{-1}$  for *Fermi*/GBM and the LIGO-Virgo-KAGRA network during O4, and Salafia et al. (2023) predicted 0.2–1.3 detectable GW-sGRB events per year for the same instruments. Similarly, Bhattacharjee et al. (2024) found rates of  $0.07$ – $0.62 \text{ yr}^{-1}$  and  $0.8$ – $4.0 \text{ yr}^{-1}$  for *Fermi*/GBM paired with IGWN4 and IGWN5, respectively. Our IGWN4 rates are also broadly consistent with Howell et al. (2019) after scaling for the higher BNS merger rate assumed in their analysis. However, the study by Patricelli et al. (2022) yielded a higher rate, which likely stems from either brighter emission models or the inclusion of Gaussian noise in GW detector simulations.

## 5 CONCLUSIONS AND DISCUSSION

In this paper, we have updated and expanded the sGRB sample detected by the *Fermi* satellite, which now includes 553 sGRBs as of

December 2023. Due to instrumental limitations in sampling faint bursts, we focused on sGRBs that are sufficiently bright in the 10–1000 keV *Fermi*/GBM energy band. Specifically, we selected bursts with a 64-ms peak photon flux of  $P \geq 4.1 \text{ photons cm}^{-2} \text{ s}^{-1}$ . Above this flux threshold, the incomplete flux sampling due to instrumental selection effects becomes negligible. Consequently, our subsample consists of 512 sGRBs with  $P \geq 4.1 \text{ photons cm}^{-2} \text{ s}^{-1}$ . Given the limited number of sGRBs with known redshifts, we estimated the pseudo redshifts of 512 sGRBs using the empirical  $E_p$ - $L$  correlation. Since the maximum redshift observed for sGRBs is 2.609, we excluded those bursts with pseudo-redshifts  $z > 3$ . As a result, we analyzed 478 sGRBs with  $P \geq 4.1 \text{ photons cm}^{-2} \text{ s}^{-1}$  and  $z \leq 3$ .

Using the sample of 478 sGRBs with  $P \geq 4.1 \text{ photons cm}^{-2} \text{ s}^{-1}$  and  $z \leq 3$ , we investigated the sGRB LF and formation rate under various delay-time distribution models. We applied the maximum likelihood method to analyze the observed redshift and luminosity distributions of the sGRB sample, and used the MCMC technology to determine the best-fit parameters for each model. We found that all delay-time distribution models seem to account for the observed redshift and luminosity distributions similarly well. Nevertheless, based on the DIC model selection criterion, the Gaussian delay model is statistically preferred, with an estimated relative probability of 99.9%. Additionally, with the best-fit parameters presented in Table 2, consistent local formation rates of sGRBs are obtained for different delay-time distribution models, i.e.,  $R_{\text{sGRB}}(0) = 1.37^{+0.30}_{-0.27} \text{ Gpc}^{-3} \text{ yr}^{-1}$  for the Gaussian delay model,  $1.63^{+0.44}_{-0.27} \text{ Gpc}^{-3} \text{ yr}^{-1}$  for the lognormal delay model, and  $1.78^{+0.12}_{-0.17} \text{ Gpc}^{-3} \text{ yr}^{-1}$  for the power-law delay model. These results are well-aligned with those of other works (Guetta & Piran 2005; Yonetoku et al. 2014; Ghirlanda et al. 2016; Paul 2018b).

Furthermore, we explored the prospects for joint detection of sGRBs and their GW counterparts from BNS mergers using three high-energy GRB detectors (*Fermi*/GBM, *SVOM*/GRM, and *EP*/WXT) and two GW detector networks (IGWN4 and IGWN5). In our analysis, the GW detection rates by the GW detector networks were estimated using the synthetic BNS population (Bhattacharjee et al. 2024). By combining the GW detection rate with the observed sGRB distributions, we further calculated the joint sGRB and GW detection rates across various GRB and GW facilities, incorporating the angular dependence of the emission energy in GRB jets. For the sensitivity of the IGWN4, the overall joint sGRB and GW detection rates are relatively low. Our predicted joint detection rates for the GRB detectors *Fermi*/GBM, *SVOM*/GRM, and *EP*/WXT with IGWN4 are 0.19–0.27, 0.07–0.10, and 0.01–0.03  $\text{yr}^{-1}$ , respectively, for different delay-time distribution models (see Columns 5–7 of Table 4). Our results offer a plausible explanation for the lack of joint sGRB and GW detection over a long period of observation due to the low joint detection rate of current instruments. Following the upgrade of the GW detection network to IGWN5, we expect to detect more sGRB-GW association events in the future. Specifically, with IGWN5, the joint detection rates would increase to 0.93–1.35, 0.51–0.79, and 0.15–0.27  $\text{yr}^{-1}$  for *Fermi*/GBM, *SVOM*/GRM, and *EP*/WXT, respectively (see Columns 8–10 of Table 4).

In this research, besides *Fermi* and *SVOM*, we also studied the sGRB detection rate of *EP*. However, *EP* is specifically designed for X-ray observation, and GRB prompt emission is not the primary aim of the satellite. As expected, *EP* does not show a strong capability in the detection of sGRBs. The observed luminosity of GRB prompt emission depends on the jet structure. In all the jet structure models, the observed luminosity decreases rapidly as the angle between the line of sight and the jet increases. Most GRBs could not be detected

due to off-axis observation. Differently, the afterglow of GRBs allows for observation from larger angles, and it is easier to detect in the X-ray band. However, there are insufficient sGRB afterglow samples to perform a study predicting the afterglow detection rate of an X-ray space telescope.

Finally, we note a caveat regarding our methodology. While we adopt the  $E_p$ - $L$  correlation for pseudo-redshift estimation throughout this work, significant systematic uncertainties affect this approach. Future refinement of redshift-estimation techniques or larger samples of sGRBs with spectroscopic redshifts will enable robust validation of our results.

## ACKNOWLEDGEMENTS

We thank the anonymous referee for their constructive comments, which greatly improved the clarity of this manuscript. We are also grateful to Dr. Shi-Jie Zheng, Dr. Guang-Xuan Lan, An Li, and Yi-Fang Liang for useful discussions. This work is partially supported by the Strategic Priority Research Program of the Chinese Academy of Sciences (grant No. XDB0550400), the National Key R&D Program of China (2024YFA1611704), the National Natural Science Foundation of China (grant Nos. 12422307, 12373053, and 12321003), and the Natural Science Foundation of Jiangsu Province (grant No. BK20221562).

## DATA AVAILABILITY

All the GRB data used in this paper can be obtained from the Fermi GBM catalog: <https://heasarc.gsfc.nasa.gov/W3Browse/fermifermigbrst.html>.

## REFERENCES

- Abbott B. P., et al., 2017, *ApJ*, **848**, L13
- Abbott R., et al., 2021, *ApJ*, **913**, L7
- Abdo A. A., et al., 2010, *ApJ*, **720**, 435
- Acernese F., et al., 2015, *Classical and Quantum Gravity*, **32**, 024001
- Ajello M., et al., 2009, *ApJ*, **699**, 603
- Ajello M., et al., 2012, *ApJ*, **751**, 108
- Aso Y., Michimura Y., Somiya K., Ando M., Miyakawa O., Sekiguchi T., Tatsumi D., Yamamoto H., 2013, *Phys. Rev. D*, **88**, 043007
- Atteia J. L., Cordier B., Wei J., 2022, *International Journal of Modern Physics D*, **31**, 2230008
- Babak S., Hewitson M., Petiteau A., 2021, *arXiv e-prints*, p. [arXiv:2108.01167](https://arxiv.org/abs/2108.01167)
- Band D., et al., 1993, *ApJ*, **413**, 281
- Barsotti L., McCuller L., Evans M., Fritschel P., 2018, The A+ design curve, <https://dcc.ligo.org/LIGO-T1800042-v4/public>
- Beniamini P., Granot J., Gill R., 2020a, *MNRAS*, **493**, 3521
- Beniamini P., Duran R. B., Petropoulou M., Giannios D., 2020b, *ApJ*, **895**, L33
- Berger E., 2014, *ARA&A*, **52**, 43
- Bhattacharjee S., et al., 2024, *MNRAS*, **528**, 4255
- Burns E., 2020, *Living Reviews in Relativity*, **23**, 4
- Chiang J., Mukherjee R., 1998, *ApJ*, **496**, 752
- Colombo A., Salafia O. S., Gabrielli F., Ghirlanda G., Giacomazzo B., Perego A., Colpi M., 2022, *ApJ*, **937**, 79
- Dainotti M. G., Petrosian V., Bowden L., 2021, *ApJ*, **914**, L40
- Dietz A., 2011, *A&A*, **529**, A97
- Dimitrova T. A., Butler N. R., Ravi S., 2023, *ApJ*, **949**, 15
- Eichler D., Livio M., Piran T., Schramm D. N., 1989, *Nature*, **340**, 126
- Faber J. A., Rasio F. A., 2012, *Living Reviews in Relativity*, **15**, 8

Fong W., et al., 2013, *ApJ*, **769**, 56

Fong W., Berger E., Margutti R., Zauderer B. A., 2015, *ApJ*, **815**, 102

Foreman-Mackey D., Hogg D. W., Lang D., Goodman J., 2013, *PASP*, **125**, 306

Ghirlanda G., et al., 2016, *A&A*, **594**, A84

Ghirlanda G., et al., 2019, *Science*, **363**, 968

Goldstein A., et al., 2017, *ApJ*, **846**, L5

Gruber D., et al., 2014, *ApJS*, **211**, 12

Guetta D., Piran T., 2005, *A&A*, **435**, 421

Guetta D., Piran T., 2006, *A&A*, **453**, 823

Guetta D., Stella L., 2009, *A&A*, **498**, 329

Hannam M., Schmidt P., Bohé A., Haegel L., Husa S., Ohme F., Pratten G., Pürer M., 2014, *Phys. Rev. Lett.*, **113**, 151101

Howell E. J., Ackley K., Rowlinson A., Coward D., 2019, *MNRAS*, **485**, 1435

Iyer B., Souradeep T., Unnikrishnan C., Dhurandhar S., Raja S., Sengupta A., 2011, LIGO-India: Proposal of the Consortium for Indian Initiative in Gravitational-wave Observations (IndIGO), <https://dcc.ligo.org/LIGO-M1100296/public>

Kaneko Y., Preece R. D., Briggs M. S., Paciesas W. S., Meegan C. A., Band D. L., 2006, *ApJS*, **166**, 298

Khan S., Husa S., Hannam M., Ohme F., Pürer M., Forteza X. J., Bohé A., 2016, *Phys. Rev. D*, **93**, 044007

Kouveliotou C., Meegan C. A., Fishman G. J., Bhat N. P., Briggs M. S., Koshut T. M., Paciesas W. S., Pendleton G. N., 1993, *ApJ*, **413**, L101

LIGO Scientific Collaboration et al., 2015, *Classical and Quantum Gravity*, **32**, 074001

Lan G.-X., Zeng H.-D., Wei J.-J., Wu X.-F., 2019, *MNRAS*, **488**, 4607

Lan G.-X., Wei J.-J., Zeng H.-D., Li Y., Wu X.-F., 2021, *MNRAS*, **508**, 52

Lan G.-X., Wei J.-J., Li Y., Zeng H.-D., Wu X.-F., 2022, *ApJ*, **938**, 129

Liddle A. R., 2007, *MNRAS*, **377**, L74

Liu H.-Y., Yu Y.-W., 2019, *Research in Astronomy and Astrophysics*, **19**, 118

Luo J.-W., Li Y., Ai S., Gao H., Zhang B., 2022, *MNRAS*, **516**, 1654

Lyman J. D., et al., 2018, *Nature Astronomy*, **2**, 751

Lynden-Bell D., 1971, *MNRAS*, **155**, 95

Margutti R., et al., 2012, *ApJ*, **756**, 63

Margutti R., et al., 2018, *ApJ*, **856**, L18

Marshall H. L., Tananbaum H., Avni Y., Zamorani G., 1983, *ApJ*, **269**, 35

Mooley K. P., et al., 2018a, *Nature*, **561**, 355

Mooley K. P., et al., 2018b, *ApJ*, **868**, L11

Nakar E., 2007, *Phys. Rep.*, **442**, 166

Nakar E., 2020, *Phys. Rep.*, **886**, 1

Nakar E., Gal-Yam A., Fox D. B., 2006a, *ApJ*, **650**, 281

Nakar E., Gal-Yam A., Fox D. B., 2006b, *ApJ*, **650**, 281

Narayana Bhat P., et al., 2016, *ApJS*, **223**, 28

Narumoto T., Totani T., 2006, *ApJ*, **643**, 81

Özel F., Freire P., 2016, *ARA&A*, **54**, 401

Pai A., Dhurandhar S., Bose S., 2001, *Phys. Rev. D*, **64**, 042004

Patricelli B., Bernardini M. G., Mapelli M., D'Avanzo P., Santoliquido F., Celli G., Razzano M., Cuoco E., 2022, *MNRAS*, **513**, 4159

Paul D., 2018a, *MNRAS*, **473**, 3385

Paul D., 2018b, *MNRAS*, **477**, 4275

Petrillo C. E., Dietz A., Cavaglià M., 2013, *ApJ*, **767**, 140

Petrov P., et al., 2022, *ApJ*, **924**, 54

Planck Collaboration et al., 2020, *A&A*, **641**, A6

Preece R. D., Briggs M. S., Mallozzi R. S., Pendleton G. N., Paciesas W. S., Band D. L., 2000, *ApJS*, **126**, 19

Salafia O. S., Ravasio M. E., Ghirlanda G., Mandel I., 2023, *A&A*, **680**, A45

Saleem M., et al., 2022, *Classical and Quantum Gravity*, **39**, 025004

Savchenko V., et al., 2017, *ApJ*, **848**, L15

Schmidt P., Hannam M., Husa S., 2012, *Phys. Rev. D*, **86**, 104063

Sieliez K., Boer M., Gendre B., 2014, *MNRAS*, **437**, 649

Sun H., Zhang B., Li Z., 2015, *ApJ*, **812**, 33

Tan W.-W., Fan X.-L., Wang F. Y., 2018, *MNRAS*, **475**, 1331

Troja E., et al., 2017, *Nature*, **551**, 71

Troja E., et al., 2018, *Nature Communications*, **9**, 4089

Troja E., et al., 2020, *MNRAS*, **498**, 5643

Tsutsui R., Yonetoku D., Nakamura T., Takahashi K., Morihara Y., 2013, *MNRAS*, **431**, 1398

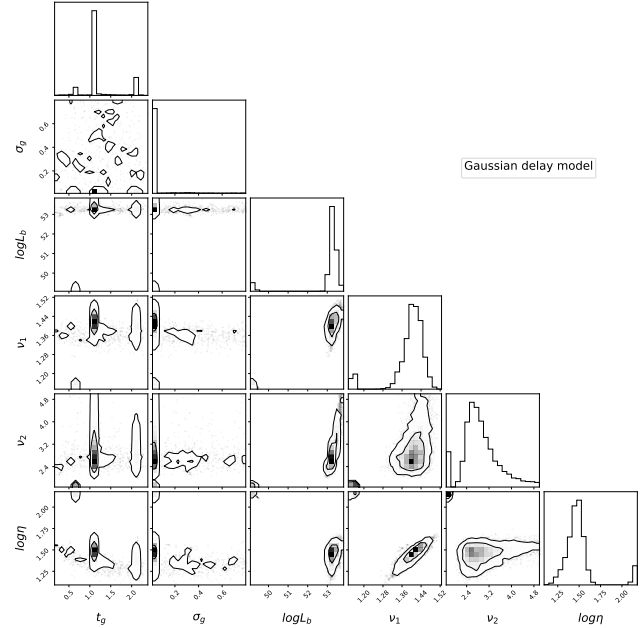


**Figure A1.** 1D posterior distributions and 2D confidence regions (with  $1-2\sigma$  contours) for the parameters of the Gaussian delay model.

Virgili F. J., Zhang B., O'Brien P., Troja E., 2011, *The Astrophysical Journal*, **727**, 109

Wanderman D., Piran T., 2015, *Monthly Notices of the Royal Astronomical Society*, **448**, 3026

Wei J., et al., 2016, *arXiv e-prints*, p. arXiv:1610.06892

Woosley S. E., 1993, *ApJ*, **405**, 273

Yonetoku D., Murakami T., Nakamura T., Yamazaki R., Inoue A. K., Ioka K., 2004, *ApJ*, **609**, 935

Yonetoku D., Nakamura T., Sawano T., Takahashi K., Toyanago A., 2014, *ApJ*, **789**, 65

Yuan W., et al., 2015, *arXiv e-prints*, p. arXiv:1506.07735

Yuan W., Zhang C., Chen Y., Ling Z., 2022, in Bambi C., Sangangelo A., eds., *Handbook of X-ray and Gamma-ray Astrophysics*. p. 86, doi:10.1007/978-981-16-4544-0\_151-1

Yüksel H., Kistler M. D., Beacom J. F., Hopkins A. M., 2008, *ApJ*, **683**, L5

Zhang G. Q., Wang F. Y., 2018, *ApJ*, **852**, 1

Zhu X., Thrane E., Osłowski S., Levin Y., Lasky P. D., 2018, *Phys. Rev. D*, **98**, 043002

von Kienlin A., et al., 2014, *ApJS*, **211**, 13

von Kienlin A., et al., 2020, *ApJ*, **893**, 46

## APPENDIX A: CORNER PLOTS OF THE MCMC INFERENCE

This paper has been typeset from a  $\text{\TeX}/\text{\LaTeX}$  file prepared by the author.

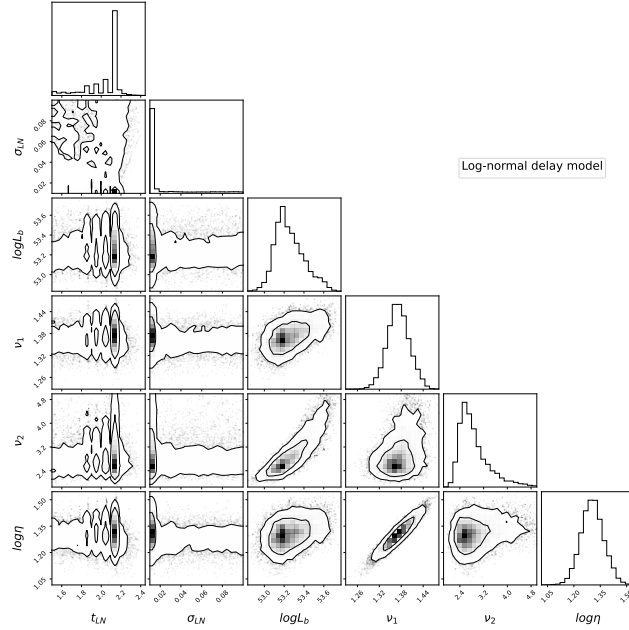


**Figure A2.** Same as Figure A1, but for the parameters of the Lognormal delay model.

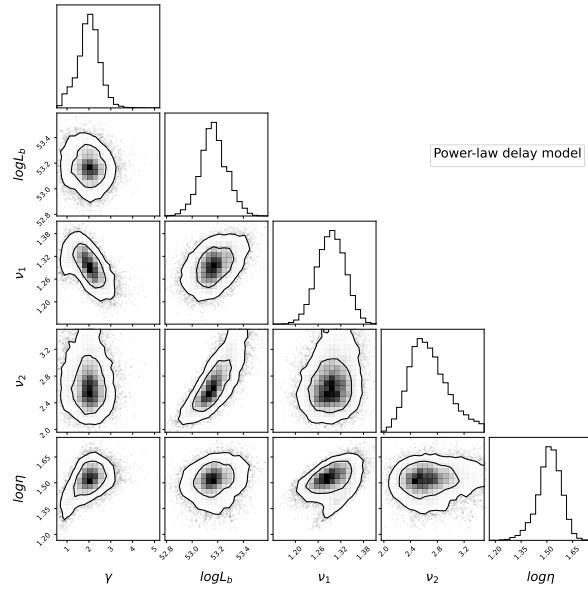


**Figure A3.** Same as Figure A1, but for the parameters of the power-law delay model.